Parameters Influencing the Photocatalytic Activity of Suspension-Sprayed TiO$_2$ Coatings

Filofteia-Laura Toma, Lutz-Michael Berger, Irina Shakhverdova, Beate Leupolt, Annegret Potthoff, Kathrin Oelschlägel, Tobias Meissner, José Antonio Ibáñez Gomez, and Yolanda de Miguel

Photocatalytic properties of titania have been studied very intensively for a variety of applications, including air and water purification. In order to clarify the influence of the phase composition and other parameters, thermal spraying with suspensions was applied to produce photocatalytically active titania coatings starting from two commercially available anatase and rutile submicron powders. Aqueous suspensions containing 40% solids by weight were sprayed with an HVOF process using ethylene as the fuel gas. The spray parameters were chosen in order to produce mechanically stable coatings and to preserve a high content of the initial crystalline phases of the powders. The coating microstructures, phase compositions, and surface properties were characterized. The photocatalytic performance was evaluated by degradation of the pink dye Rhodamine B (RB) using two techniques: degradation of an aqueous solution of RB and discoloration of impregnated RB. All the coatings exhibited photocatalytic activity to varying degrees, depending on the phase composition as well as other factors, namely, the coating microstructure, surface morphology, surface hydroxylation, light absorption, and interaction with the pollutant.

1. Introduction

1.1 Photocatalysis: TiO$_2$ Photocatalyst

In recent years, photocatalysis has been the focus of intensive research activities covering a variety of applications and products in the environmental and energy fields. In 1972, Fujishima and Honda (Ref 1) reported the phenomenon of photocatalysis on titanium dioxide (TiO$_2$) and the development of the photoelectrochemical cell for solar energy conversion and water photolysis on TiO$_2$ electrodes. This work, initiated during the oil crisis in the 70s, aimed to develop artificial systems capable of converting solar energy into chemical or electrical energy.

The materials most commonly used as photocatalysts are semiconductors, but they have to be active, capable of

using the energy spectra of visible light and near-ultraviolet light, biologically inert and nontoxic, environmentally friendly, chemically stable with no photo-corrosion, virtually insoluble in water, and cost-effective. When a semiconductor catalyst of the chalcogenide type oxide (TiO$_2$, ZnO, SnO$_2$, CeO$_2$, Fe$_2$O$_3$, SrTiO$_3$, etc.), sulfide (CdS, ZnS, etc.), or selenide (CdSe) is illuminated with photons whose energy is equal to or greater than its band gap energy E_g (hν $\geq E_g$), absorption of the photons and formation of photogenerated charge carriers, i.e., holes in the valence band and electrons in the conduction band, occurs in the bulk of the material (Fig. 1; Ref 2). These species are very reactive and can follow different paths: the undesired recombination of electrons and holes or the diffusion/transfer of electrons and holes from the bulk to the material surface, where they interact with the adsorbed water and oxygen molecules. The oxidation of water or HO ions by photogenerated holes produces hydroxyl radicals ($\cdot$OH) that react with the adsorbed pollutants. The photogenerated electrons participate in reduction processes, typically reacting with molecular oxygen to produce superoxide anions or radicals of O$_2$.

The ability of a semiconductor to undergo photoinduced electron/hole transfer to adsorbed species on its surface is governed by the band energy positions of the semiconductor and the redox potentials of the adsorbates. The conduction band potential of the semiconductor is thermodynamically required to be more negative than the reduction potential level of the adsorbed acceptor species in order for it to participate in photoreduction reactions. Similarly, the potential of the valence band of the

Filofteia-Laura Toma, Lutz-Michael Berger, Irina Shakhverdova, and **Beate Leupolt**, Fraunhofer Institute for Material and Beam Technology (IWS), Dresden, Germany; **Annegret Potthoff, Kathrin Oelschlägel,** and **Tobias Meissner**, Fraunhofer Institute for Ceramic and Sintering Technologies (IKTS), Dresden, Germany; and **José Antonio Ibáñez Gomez** and **Yolanda de Miguel**, TECNALIA, Parque Tecnológico de Bizkaia, Derio, Bizkaia, Spain. Contact e-mail: filofteia-laura.toma@iws.fraunhofer.de.

Fig. 1 Schematic representation of the photocatalytic mechanism (redrawn from Ref 2, 6)

semiconductor needs to be more positive than the oxidation potential of the adsorbed donor species in order for it to participate in photooxidation reactions (Ref 3). Production of hydroxyl radicals from H_2O and reduction of O_2 require a material with a band gap of around 3 eV. Due to its appropriate valence and conduction band positions, TiO_2 is the most preferred photocatalytic material.

TiO_2 photocatalysis has been extensively reported in development and testing of products for water splitting and hydrogen evolution, self-cleaning surfaces, air and water purification systems, sterilization, and photoelectrochemical cells (see, e.g., Ref 4-6). Both TiO_2 crystalline forms, anatase and rutile, have been studied for photocatalytic applications. A general consensus places the band gaps of rutile and anatase TiO_2 at 3.03 and 3.20 eV, respectively (Ref 7, 8). Nonetheless, for the same crystalline structure of the TiO_2, various band gap energy values are reported in the literature (see, e.g., Ref 9-12). These values depend on different intrinsic and extrinsic properties of the TiO_2 linked to the method of powder preparation, particle sizes, degree of crystallization, presence of defects, doping of TiO_2, method of coating deposition, and so on.

It is generally assumed that anatase is more reactive than rutile due to its higher Fermi energy and higher surface hydroxylation rate. In contrast, the commercial P25 Degussa TiO_2 powder, which is nanocrystalline and contains ~80 vol.% anatase and ~20 vol.% rutile, displays a higher activity than rutile or anatase. In the mixture, the electron/hole separation is supposed to be favored by the polyphasic nature of the particles. In order to explain the photocatalysis mechanism on P25 particles, Hurum et al. (Ref 13, 14) proposed two models: (i) the rutile acts as a trap for electrons generated by the action of the light in the anatase phase and (ii) the rutile acts as an antenna to absorb light and the photogenerated electrons in rutile are trapped by anatase. Consequently, the distance between the electron-hole pairs increases, the recombination of the electrons and holes is limited, and therefore the photogenerated species are involved in the oxidation-reduction reactions on the surface of the catalyst. Other authors (Ref 8, 15) proposed an energetic alignment of the bad edges of the rutile and the anatase, with anatase possessing the higher electron affinity. This alignment facilitating

an efficient electron-hole separation is likely the driving force for the increased photoactivity of anatase-rutile composites compared with their individual counterparts. Nonetheless, the optimum composition of the two phases for the photocatalytic reactions has not been completely clarified yet. In addition to the phase composition, the particle sizes and the presence of impurities on the particle surface are also expected to influence the photocatalytic ability of the titania.

For water purification, titanium dioxide can be used in the form of slurry or immobilized in the form of a film or a coating deposited by different techniques such as sol-gel, dip-coating, or physical or chemical vapor deposition. TiO_2 powders have an outstanding photocatalytic efficiency compared with the coatings due to their higher specific surface area. However, the separation of the powder from the liquid state used in water treatment and recycling processes is troublesome. On the other hand, it is supposed that the aforementioned difficulties concerning films and coatings can be overcome and their application areas can also be expanded through employment of different materials as substrates. For air purification or for preparation of the self-cleaning surfaces, a mechanically stable thin coating is needed.

1.2 Thermal Spraying and Photocatalysis

Thermal spraying technology is largely used to produce titanium oxide coatings for mechanical, tribological, electrical, and biomedical applications as well as for sputter targets (Ref 16). Over the last decade thermal spraying for the preparation of coatings with effective photocatalytic performance has been gaining in interest. Titanium oxide coatings prepared by atmospheric plasma spraying (APS), high velocity oxy-fuel spraying (HVOF), or water-stabilized plasma spraying (WSP) have been tested with a wide variety of pollutants, including acetaldehyde (Ref 17-19), acetone (Ref 20, 21), ammonia (Ref 22), nitrogen oxides (Ref 23-25), methylene blue (Ref 26-28), phenol (Ref 29), or rhodamine B (Ref 19). With only a few exceptions, the photocatalytic responses were relatively low. The main issue was the irreversible phase transformation of anatase to rutile that occurred during the thermal spray process. Numerous efforts have been made to preserve a higher amount of anatase in the coatings. Very promising results were obtained for TiO_2 coatings sprayed using suspensions as feedstock materials with both APS and HVOF techniques (see, e.g., Ref 19, 24, 25, 30-35) or cold spray processes (see, e.g., Ref 36-39).

Although it is generally agreed that the anatase phase is the most active phase and has to be preserved in the sprayed coatings, several authors confirmed that titania coatings containing rutile as the main phase were photocatalytically active (Ref 20, 28, 34, 35). Regarding the photocatalytic performance of sprayed TiO_2 coatings, attention has to be paid to the procedure and compound(s) used for the evaluation of the photocatalytic activity: nature of the molecule to be degraded and its complexity, state (gaseous, liquid, impregnated) and concentration of the pollutant, physicochemical interaction of

the pollutant with the coating, stability of the pollutant when light irradiated, UV lamp type (source, power, light intensity, emission light spectrum), and type (batch or continuous) and duration of the test. Several authors (Ref 19, 30, 38, 39) showed that the coating can present different photocatalytic responses when its activity is evaluated by the degradation of various pollutants. Consequently, because of the aforementioned difficulties, the applications of a ''universal photocatalytic test'' as well as the production of a ''universal photocatalytic coating'' are still topics of intensive scientific research.

The work reported in this paper involves a study of the microstructure, phase composition, surface properties, and photocatalytic performance of titania coatings produced from aqueous suspensions of two commercially available submicron TiO_2 powders. The coatings were produced on sand-blasted stainless steel plates and on porous ceramic substrates using HVOF spraying. The aim was the evaluation of the influence of the suspension and the spray parameters, i.e., gas flow rates, oxygen-to-fuel ratio, and spray distance on the microstructure and phase composition of the coatings and the photocatalytic ability of the nanostructured coatings to degrade the pink dye Rhodamine B (RB). An attempt was made to correlate the spray parameters with the coating properties and with the methods used for the photocatalytic degradation of RB.

2. Materials and Experimental Procedures

2.1 Feedstock Powders and Suspensions Preparation

Two commercially available submicron-sized TiO_2 powders (Sachtleben Chemie GmbH, Duisburg, Germany) with different phase compositions and particle sizes were used to produce the sprayable aqueous suspensions: a 99.7 wt.% anatase powder (trade name: Hombikat N10) with an average particle size d_{50} of about 900 nm and a 98.5 wt.% rutile powder (trade name: Rutile R320) with d_{50} around 500 nm. The properties of the TiO_2 powders are summarized in Table 2.

The particles size distributions of the raw powders were measured by laser diffraction using a Mastersizer 2000 (Malvern Instruments GmbH, Herrenberg, Germany). The powder densities were determined by helium pycnometry using a Penta-Pyknometer (Quantachrome GmbH & Co., Odelzhausen, Germany). The specific surface area of the as-received powders was determined by nitrogen adsorption using the Brunauer-Emmett-Teller (BET) theory (ASAP 2000 apparatus, Micromeritics GmbH, USA).

Colloidally stable and well-dispersed suspensions with low viscosity, low sedimentation rate, and no corrosive effects on the spray equipment are indispensable for the long-term stability and the efficiency of the spray process (Ref 40, 41). Aqueous suspensions of both powders were obtained by dispersion and homogenization of 40 wt.% powder in deionized water. A small quantity of diammo-

nium citrate (up to 0.2 wt.%/wt.% powder) was added as a dispersing agent in order to increase the stability of the anatase-based suspension. The stability of the rutile suspension was improved by adjustment of the pH value to 4-5. The dynamic viscosities of the suspensions were measured with an MCR 101 rheometer (Anton Paar GmbH, Graz, Austria). The electrostatic stability was determined by zeta potential measurements using a Zeta Analyser™ (Colloidal Dynamics, FL, USA), whereas the sedimentation rates were analyzed by laser light scattering with a LUMISizer® apparatus (L.U.M. GmbH, Berlin, Germany).

2.2 Suspension Thermal Spraying

The suspensions were sprayed by an HVOF TopGun (GTV mbH, Luckenbach, Germany) with a nozzle of diameter 8 mm and ethylene as the fuel gas. A modified combustion chamber allowing axial injection of the suspension was adapted to the HVOF gun. Suspensions were fed from a pressurized vessel using the laboratory setup (Ref 41). The pressure in the reservoir, between 0.25 and 0.35 MPa, was chosen in such a way that good penetration of the liquid feedstock into the supersonic flame was ensured. For the coating deposition, the main variable parameters were the gas flow rates, normalized oxygen-to-fuel ratio (λ), and spray distance (Table 1). These parameters were selected to preserve the initial phases and at the same time to ensure the preparation of mechanically stable coatings. The coatings were sprayed on sand-blasted stainless steel plates using corundum (EKF 40, sand blasting pressure of 4 bar) as well as on porous ceramic tile substrates (K2, INAX Corporation, Aichi, Japan). The samples were air cooled with air jets during spraying.

2.3 Structural Characterization

The morphologies of the raw powders and the microstructures of the metallographically prepared cross sections of the suspension-sprayed coatings were examined using a JEOL JSM 6610 scanning electron microscope (SEM). High-magnification micrographs were obtained using a focused ion beam (FIB) Gemini 982 SEM microscope (Carl Zeiss NTS GmbH, Oberkochen, Germany).

X-ray diffraction in the step-scan mode (Bruker D8 Advance diffractometer, Bruker AXS GmbH, Karlsruhe, Germany) using monochromatic Cu Kα radiation in the 10°-90° 2θ range with a scan step of 0.03° was used to assess the anatase-to-rutile ratio. The anatase content was determined using the Rietveld method.

The presence of the different crystalline phases at the top surface of the as-sprayed coatings was investigated by Raman spectroscopy performed with a Renishaw 3000 Raman microscope (Renishaw GmbH, Pliezhausen, Germany) at a laser wavelength of 514 nm and an integration time of 60 s. The localization of the analysis spot of the laser was performed using an optical microscope with an objective with a magnification of 50×.

Table 2 Spray parameters and coating properties

TiO$_2$ Suspension	Sample	Spray parameters						Surface roughness			
		C$_2$H$_4$, L/min	O$_2$, L/min	λ	SD, mm	Passes	Substrate	Average thickness, µm	R_a, µm	R_z, µm	Anatase content, wt.%
40 wt.% N10	N1	50	180	1.2	70	10	Metallic	155 ± 10	2.9 ± 0.2	19.4 ± 0.6	55.0
	N2	60	180	1.0	80	10		195 ± 10	5.0 ± 0.4	32.7 ± 3.2	54.2
	N3	50	180	1.2	80	6	Ceramic	80 ± 5	4.5 ± 0.3	23.5 ± 1.9	55.1
	N4	40	150	1.3	80	6		60 ± 5	4.4 ± 0.5	22.9 ± 3.3	62.2
	N5	50	180	1.2	90	8		95 ± 5	4.6 ± 0.8	24.6 ± 3.0	56.4
	N6	40	150	1.3	90	8		75 ± 10	4.6 ± 0.7	23.4 ± 1.6	64.5
40 wt.% R320	R1	50	180	1.2	70	10	Metallic	155 ± 5	2.7 ± 0.2	17.0 ± 1.4	20.2
	R2	50	180	1.2	100	4		40 ± 5	3.2 ± 0.1	21.0 ± 1.4	17.8
	R3	40	150	1.3	90	8	Ceramic	55 ± 5	2.7 ± 0.3	25.5 ± 4.8	6.5
	R4	50	180	1.2	90	8		110 ± 5	4.2 ± 0.2	21.2 ± 4.2	17.9

SD, spray distance. $\lambda = \dfrac{\textbf{Flow rate of O}_2\left(\frac{l}{\textbf{min}}\right)}{3\times\textbf{Flow rate of C}_2\textbf{H}_4\left(\frac{l}{\textbf{min}}\right)}$

2.4 UV-Vis and IR Spectroscopy Characterization

UV-Vis light absorption of powders and as-sprayed coatings was determined by diffuse reflectance measurements using a Zeiss MCS 400 UV-Vis-NIR spectrometer (Carl Zeiss MicroImaging GmbH, Germany).

The presence of the adsorbed species on the surfaces of the powders and coatings was identified from diffuse reflectance infrared spectra recorded at wavelengths between 1.28 and 25 µm at room temperature and under atmospheric conditions using a Spectrum 2000 FTIR spectrometer (PerkinElmer Inc., Massachusetts, USA).

2.5 Photocatalytic Activity Measurements

The photocatalytic performance of the suspension-sprayed coatings was evaluated by degradation of the pink dye Rhodamine B (RB) using two different methods:

– The first method was based on the degradation of an aqueous solution of RB in the presence of the TiO$_2$ coatings.
– The second method was based on the colorimetric measurements of the TiO$_2$ coating surfaces impregnated by RB. This test enables a qualitative estimation of the self-cleaning ability of a surface to be made.

All the tests were performed on as-sprayed coatings with substrates.

In the first method, the coatings (4.5 × 4.5 cm^2) were placed into 100 mL of a 10^{-5} mol/l RB solution and irradiated for 6 h with a black light mercury UVA HSW 400 lamp with an input light power of 400 W and an irradiance of 1.2 W/m^2 (Havells Sylvania Germany GmbH, Erlangen, Germany). During the test, the samples were continuously cooled with a fan to avoid heating due to light irradiation. The degradation of the RB was monitored by absorbance measurements at a wavelength of 554 nm (which corresponds to the maximum absorption of the RB peak) using a DR 5000 UV-Vis spectrophotometer (HACH LANGE GmbH Berlin, Germany). Before irradiation, the RB solution with the coating was kept in the dark for 30 min to allow the RB to be adsorbed on the coating surface, after which time the RB concentration was determined. A blank test consisting in the irradiation of the RB solution without coating was performed to evaluate the degradation of the RB due to the photolysis phenomenon. From the absorbance values measured after each 30 min of UV irradiation, the concentration of the RB was determined following the Beer-Lambert law.

In the second photocatalytic method, the coatings (4.5 × 4.5 cm^2) that were previously impregnated with a RB solution (0.1 g RB in 100 mL dichloromethane) were placed into a QUV Accelerated Weathering Tester (Q-Lab Corporation, Cleveland, OH, USA) equipped with four UV fluorescent UVA-340 lamps (wavelength between 315 and 400 nm) with an emission peak at 340 nm (lamp power of 40 W and irradiance of about 0.7 W/m^2). The photocatalytic discoloration of RB was followed by colorimetry using a GretagMacbeth CE-XTH spectrophotometer (X-Rite Europe GmbH, Regensdorf, Switzerland). The results were expressed in the CIE LAB system by the color tonality ($a*$) measured during UV irradiation. The values of $a*$ were obtained directly from the spectrophotometer over a period of 2 h at 10 min intervals for the first hour and after 60 min for the second hour. A blank test consisting in impregnation of the dye into the uncoated ceramic substrate and irradiation of the sample under the same conditions as for the coatings was also performed.
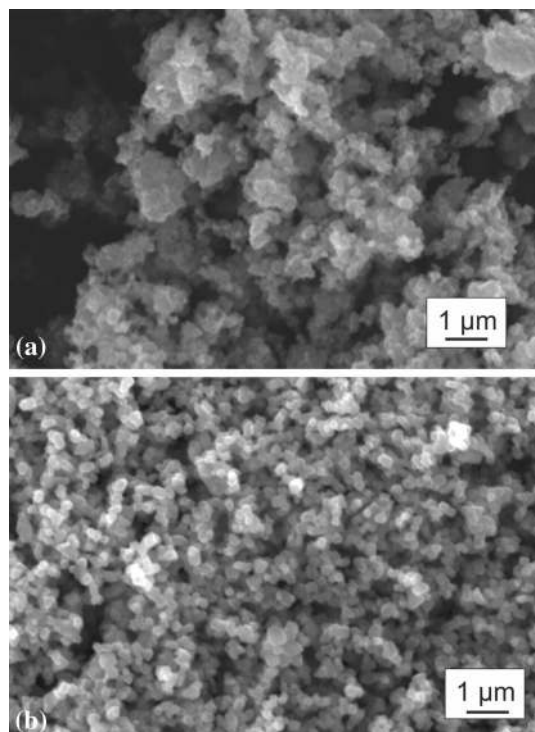
3. Results

3.1 Powder and Suspension Characteristics

The powder properties were determined and compared with the product certification data sheets (Table 2). Contrary to the manufacturer's data, a small amount of rutile phase (about 3%) was detected in the anatase powder. By laser diffraction, the average $d_{50,3}$ particles sizes were measured at 830 and 440 nm for anatase and rutile, respectively. The crystallite sizes were calculated

Table 2 Feedstock powder properties

Powder properties	Anatase (N10)	Rutile (R320)
Purity, %	> 99.7(a)	> 98.5(a)
Crystallinity	Anatase + 3% rutile	Rutile
Crystallite size, nm	142 (Anatase)	232
	170 (Rutile)	
Density, g/cm^3	3.9	4.2
Average particle size $d_{50,3}$, nm	830	440
Specific surface area, m^2/g	11.8	7.0

(a) According to product certification data

Fig. 2 SEM micrographs showing the morphologies of as-received powders: (a) anatase N10; (b) rutile R320

using the XRD diffraction results and the Scherrer equation. In the anatase powder, the crystallite size of anatase was 142 nm and the crystallite size of rutile was 170 nm. In the rutile powder, the crystallite size was determined to be 232 nm. SEM micrographs showing powder morphologies are shown in Fig. 2. Compared with rutile powder, the anatase powder has a higher tendency to agglomerate.

Very stable suspensions with high powder content (40 wt.%), low viscosities, and low sedimentation rates were prepared from both powders. The suspensions were electrostatically stabilized. The zeta potential was about—50 mV for the anatase suspension and—40 mV for the rutile suspension. The dynamic viscosities at a shear rate of 100 s^{-1} were 2 and 3 mPa s for the anatase and rutile suspensions, respectively. The sedimentation rate was less than 5 μm s^{-1} for both suspensions.

3.2 Coating Microstructures

Mechanically stable coatings with thicknesses ranging from 40 μm to about 200 μm were produced. Compared with the conventional coatings, the suspension-sprayed coatings showed smoother surfaces with average roughness R_a values varying from 2.7 to 5.0 μm and with average maximum height roughness R_z values ranging from 17.0 to 32.7 μm, the highest values being yielded for the anatase coatings (Table 1). Spraying with the higher energy HVOF flame (higher C_2H_4 flow rate) or at a larger spray distance resulted in a slightly higher surface roughness.

The coating microstructures were sensitive to the spray parameters. The variation in the cross-sectional microstructure as a function of the gases and spray distances is illustrated by the micrographs in Fig. 3 and 4. Dense structures containing well-melted particles were produced when higher C_2H_4 (C_2H_4/O_2) flow rates and very small spray distances of 70 mm were used, as observed in the N1 and R1 coatings. At high magnification, some regions containing agglomerates of fine grains with sizes between 100 and 200 nm coming probably from the dried suspension droplets and resulting particles into the HVOF flame (Ref 42, 43) were observed. Spraying at short distances resulted in some cracks parallel to the substrate because of the cooling stresses as well as vertical cracks coming from high relaxation stresses. The presence of these cracks seems to be more evident in rutile coatings.

With increasing spray distance, the amount of regions of finely agglomerated particles in the matrix of well-melted particles increased. The coatings showed a bimodal structure, as could be seen, for example, in the cross sections of the N5 and R4 coatings. The bimodal microstructures, which were already mentioned in previous studies (Ref 19, 35), were indicated by light gray regions containing well-melted particles intimately mixed with dark gray regions of unmelted nanoparticles or already solidified grains with sizes of around 100 nm.

When the coatings were sprayed at a low fuel flow rate (i.e., 40 l/min C_2H_4 and λ of 1:3) and the substrates were fixed at larger spray distances, the presence of regions with nanoagglomerated particles was more evident, as could be seen in the N6 and R3 coatings. When the suspension was sprayed with low-energy spray conditions, less heat transfer from the HVOF flame to the particles occurred, resulting in retention of a higher amount of nano-sized particles.

The SEM micrographs of the top surfaces of selected coatings for different spray parameters (gases and spray distances) are shown in Fig. 5. The presence of fine micron-sized splats coming from well-melted particles and tiny agglomerated submicron or nano-sized particles resulted from unmelted or partially melted particles, as already observed in the cross sections. When the coating was sprayed at a large spray distance, i.e., 100 mm (R2 coating), submicron and micron-sized spherical particles coming from the melted particles that cooled in flight before reaching the substrates as well as very fine unmelted nanoparticles were predominantly on the coating surface.
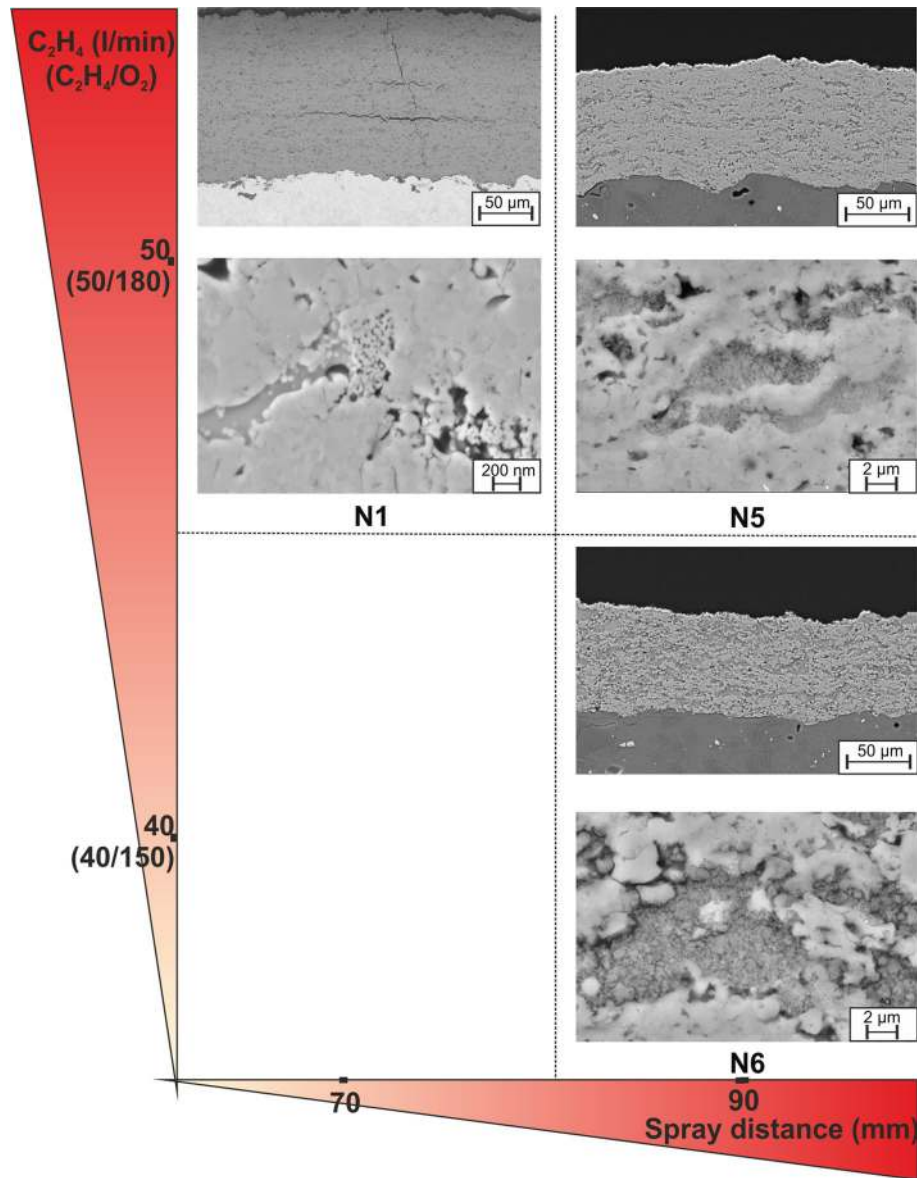
Fig. 3 SEM micrographs of cross sections of selected anatase coatings at different magnifications

3.3 Phase Compositions

In all coatings, mixtures of both anatase and rutile were identified by x-ray diffraction. In the coatings produced from the anatase suspension, anatase was retained as the major crystalline phase (55-65 vol.%), as shown in Table 1. Increasing the ethylene flow rate (from 40 to 60 l/min) and the total flow rates resulted in a slight decrease in the anatase content in the coatings. Increasing the spray distance (from 70 to 90 mm) yielded nearly no change in the anatase/rutile ratio.

Rutile was mainly found in the coatings sprayed from the rutile suspension. The anatase contents varied from 6.5 to 20 vol.% but were significantly higher than reported in a previous work (see, e.g., Ref 34). Contrary to the anatase coatings, the rutile coatings exhibited an increase in the anatase content with increasing C_2H_4 flow rate. Larger spray distances yielded lower anatase contents.

Whereas the feedstock powders were white, the coatings varied from light blue when sprayed at a low C_2H_4 flow rate and a large spray distance to gray when sprayed at a high ethylene flow rate and a smaller spray distance. The change in color was likely induced by the appearance of substoichiometry in the TiO_2 (TiO_{2-x}) (Ref 16), but the extent could not be determined from the XRD diffraction patterns of the coatings.

Raman spectroscopy was used for determination of the crystalline phases on the coating surfaces (Fig. 6). The strong peaks at 144, 397, 516, and 639 cm^{-1} in addition to weak peaks at 198 and 795 cm^{-1} corresponded to active Raman modes of the anatase (Ref 32, 44). The Raman modes for the
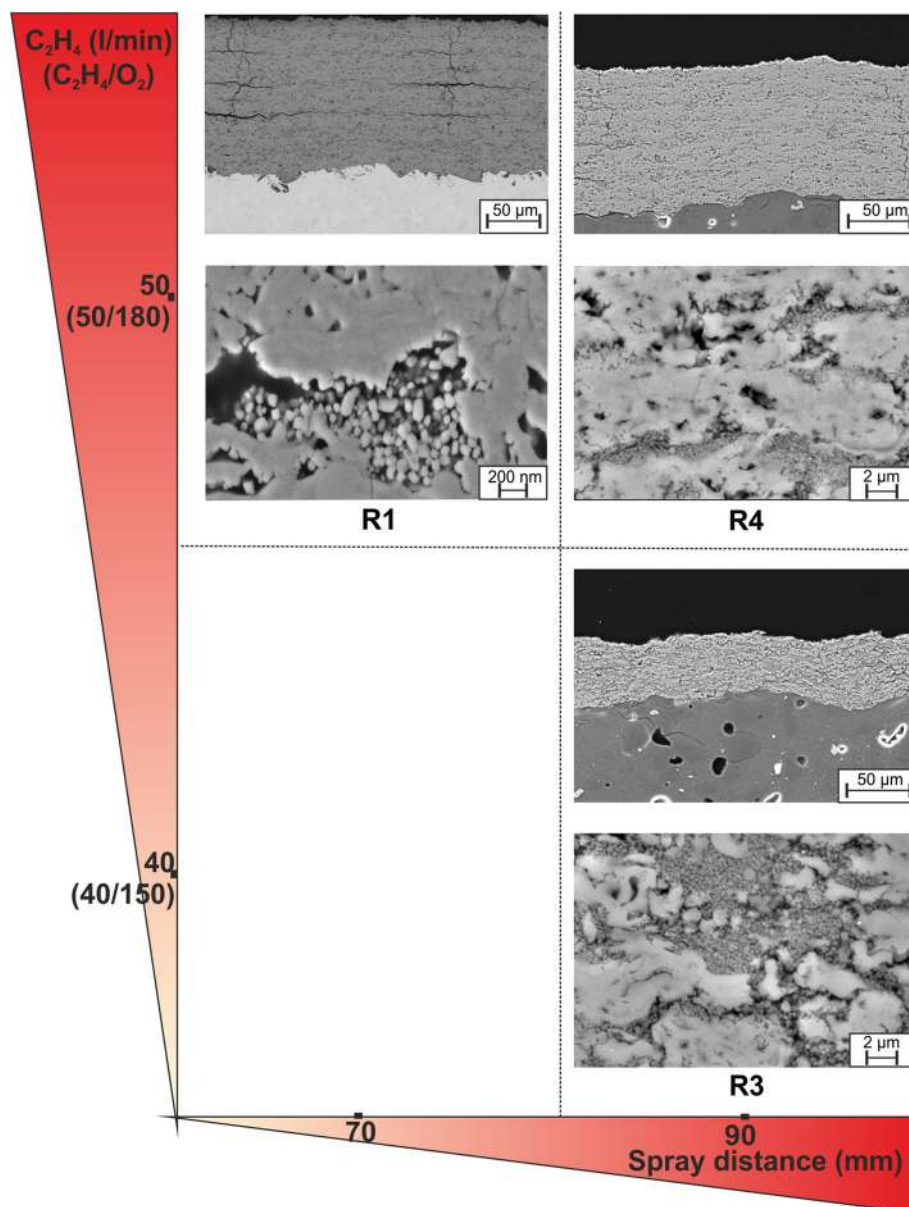
Fig. 4 SEM micrographs of cross sections of selected rutile coatings

rutile phase were given by strong peaks at 449 and 610 cm^{-1} and weak, broader peaks at 235, 320, and 832 cm^{-1}. The anatase phase was mainly found for coatings produced from the anatase suspension (Fig. 6a), confirming the XRD results, whereas the rutile phase was mostly identified on coatings sprayed from the rutile suspension (Fig. 6b).

3.4 UV-Vis Spectroscopy

The UV-Vis diffuse reflectance spectra of selected coatings and the raw powders are shown in Fig. 7. For the anatase coatings, the maximum reflectance was shifted to higher wavelengths from those of the raw anatase powder (Fig. 7a). This displacement could be explained by the presence of the rutile phase in the coatings. In contrast, for the rutile coatings in comparison with the rutile powder,

the reflectance was slightly shifted to lower wavelength values (Fig. 7b), probably due of the presence of anatase. In all cases, the reflectance was significantly lower in the coating than in the respective feedstock powder. This can be explained by the light scattering due to the heterogeneous coating microstructure.

The values of the reflectance can be converted to absorbance α using the Kubelka-Munk remission function (Ref 9) using the following equation:

$$F(R_\infty) = \frac{(1 - R_\infty)^2}{2R_\infty} \cong \alpha, \tag{Eq 1}$$

where R_∞ is the reflectance of an infinitely thick sample with respect to a reference at each wavelength and α is the absorption coefficient.
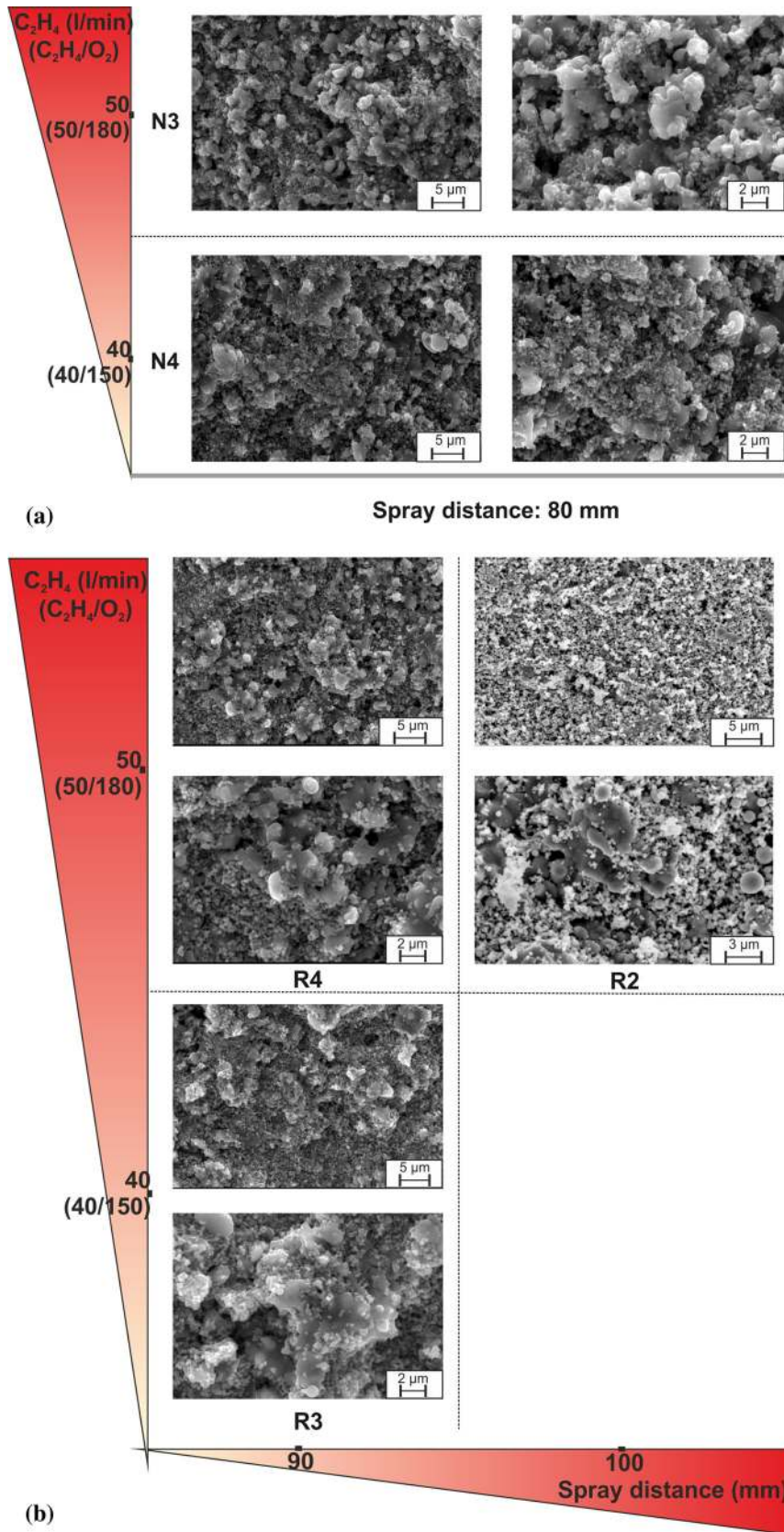
Fig. 5 SEM morphologies of top surfaces of selected: (a) anatase coatings; (b) rutile coatings
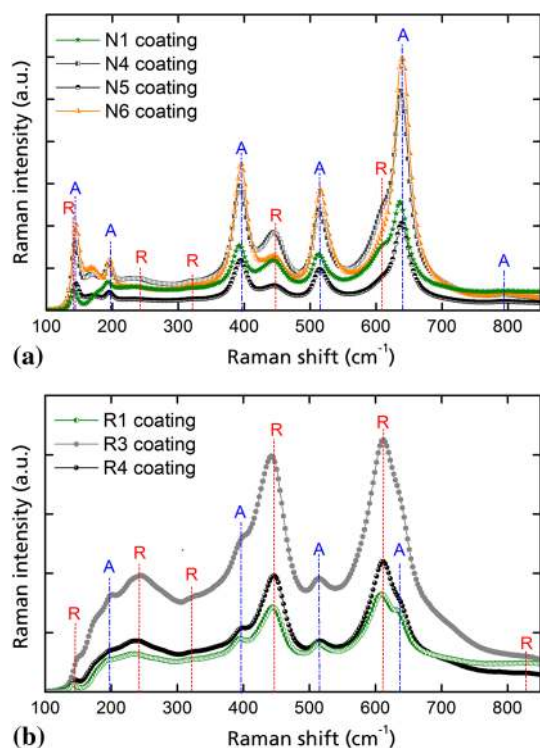
Fig. 6 Raman spectra of selected coatings: (a) from anatase suspension; (b) from rutile suspension ("A" denotes the anatase phase and "R" the rutile phase)
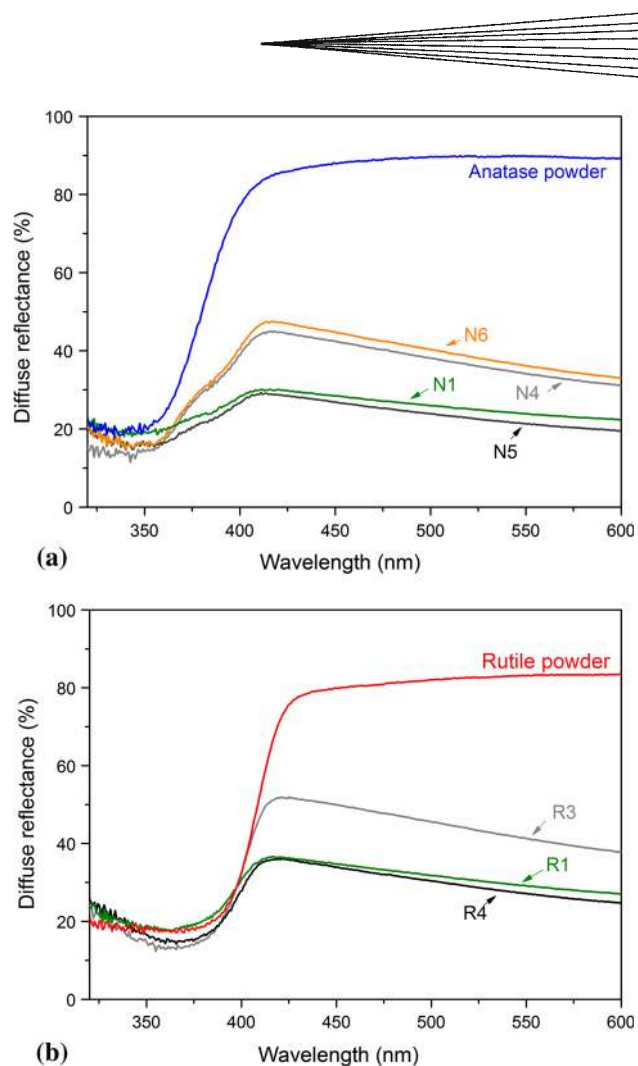

Fig. 7 UV-Vis diffuse reflectance spectra of selected coatings compared with the feedstock powders: (a) anatase coatings; (b) rutile coatings

Equation 1 is valid presuming that the light scattering on the samples is constant at all measured wavelengths.

The graphs of absorption coefficient versus photon energy can be used to determine the type of electron transitions from valence band to conduction band, i.e., direct or indirect transitions, as well as the value of the band gap E_g (Ref 9, 45).

A direct band gap, where the electrons are transferred directly from the highest energetic level in the valence band to the lowest energetic level in the conduction band, follows the law:

$$(\alpha E_{photon})^2 = A(E_{photon} - E_g) \qquad \text{(Eq 2)}$$

with

$$E_{photon}(eV) = h\nu = \frac{1239}{\lambda}, \qquad \text{(Eq 3)}$$

where E_{photon} is the photon energy determined at each wavelength (λ) and A is the slope of the linear region in the plot $(\alpha E_{photon})^2$ versus E_{photon} and the extrapolation to $\alpha = 0$ of which yields the direct E_g.

On the other hand, an indirect band gap usually follows the Tauc law:

$$(\alpha E_{photon})^{1/2} = B_{Tauc}(E_{photon} - E_g), \qquad \text{(Eq 4)}$$

where B_{Tauc} (Tauc parameter) is the slope of the linear region in the plot $(\alpha E_{photon})^{1/2}$ versus E_{photon}. The extrapolation of the E_{photon} value to $\alpha = 0$ gives the

absorption energy, corresponding to the indirect band gap E_g. According to Eq 4, the optical gap (absorption edge) can be determined.

It should be noted that these relationships are only valid for parabolic bands and are hence only physically meaningful for values of photon energies not much larger than the band gap energy, in which cases the absorption is not very strong.

The plots of $(\alpha E_{photon})^2$ and $(\alpha E_{photon})^{1/2}$ versus the photon energy for direct and indirect transitions in powders and selected coatings are shown in Fig. 8. Band gaps E_g for direct and indirect transitions are obtained by extrapolation to $\alpha = 0$.

The anatase powder has an $E_{g,direct}$ of about 3.31 eV and an $E_{g,indirect}$ of 3.12 eV. The rutile powder has an $E_{g,direct}$ of about 3.10 eV and an $E_{g,indirect}$ of 2.94 eV. According to Reyes-Coronado et al. (Ref 9), an indirect transition is relevant for anatase, whereas a direct transition is mostly found in rutile. Moreover, different authors (Ref 45, 46) showed that the anatase can present a direct transition in the case of nanostructured materials.
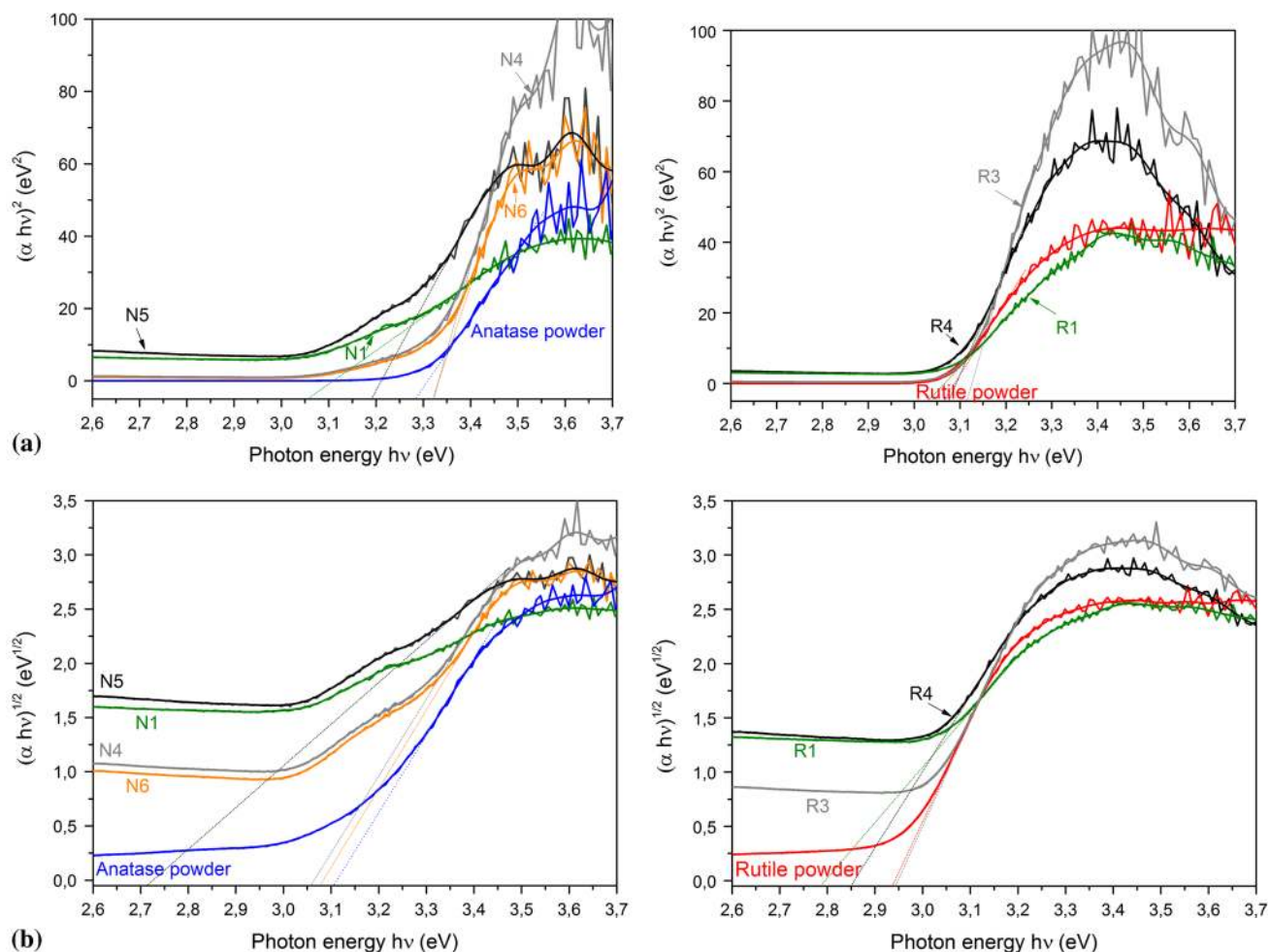
Fig. 8 (a) Plots of $(\alpha \cdot h\nu)^2$ vs. the photon energy ($h\nu$) for direct transitions in powders and selected coatings; (b) plots of $(\alpha \cdot h\nu)^{1/2}$ vs. the photon energy ($h\nu$) for indirect transitions in powders and selected coatings (band gaps E_g for direct and indirect transitions are obtained by extrapolation to $\alpha = 0$)

For the anatase coatings, the plots mostly showed two peaks, probably indicative of the presence of intermediate band transitions in the various parts of the band structure. Considering only the fitted straight slope at higher photon energy, the values of $E_{g,direct}$ of anatase coatings were between 3.06 and 3.30 eV and those of $E_{g,indirect}$ were between 2.73 and 3.08 eV. For coating N1, because of a low number of fitting points, determination of $E_{g,indirect}$ was not possible. For the rutile coatings, $E_{g,direct}$ was estimated to be between 3.06 and 3.12 eV and $E_{g,indirect}$ varied from 2.80 to 2.95 eV. The band gap energies of the anatase coatings were shifted to lower values from that of the anatase powder, whereas the band gap of rutile coatings were shifted to higher values from that of the corresponding powder. As for the rutile coatings, the direct transitions seem to be more favorable in the anatase coatings.

3.5 Infrared Spectroscopy

Figure 9 presents the IR spectra of the raw powders and the different coatings. The IR spectra of the powders

(Fig. 9a) were characterized by an intense large band in the 3800-2700 cm^{-1} region centered at 3300 cm^{-1} with emergent peaks at 3700 and 3670 cm^{-1}, a band between 1800-1500 cm^{-1} with peaks at 1640 and 1616 cm^{-1}, and a band in the 1300-700 cm^{-1} region centered at 1070 cm^{-1}. The peak at 3690 cm^{-1} corresponded to the hydroxyl groups chemisorbed on the crystalline surfaces of the titania or the defects (Ref 31). The broad band between 3650 and 2600 cm^{-1} could be attributed to the OH stretching of water molecules (physisorbed molecular water), whereas the band centered at about 1630 cm^{-1} was assigned to their bending mode. In the case of the rutile powder, the bands observed between 2990 and 2870 cm^{-1} were due to the presence of organic contaminants, most likely corresponding to the additive compounds from powder manufacturing. The peaks located in the range 2400-2300 cm^{-1} could be associated with CO_2 from air. The band centered at 1070 cm^{-1} was due to the Ti-OH and Ti-O groups.

The IR spectra of the coatings were different from those of powders (Fig. 9b and c). The band located at
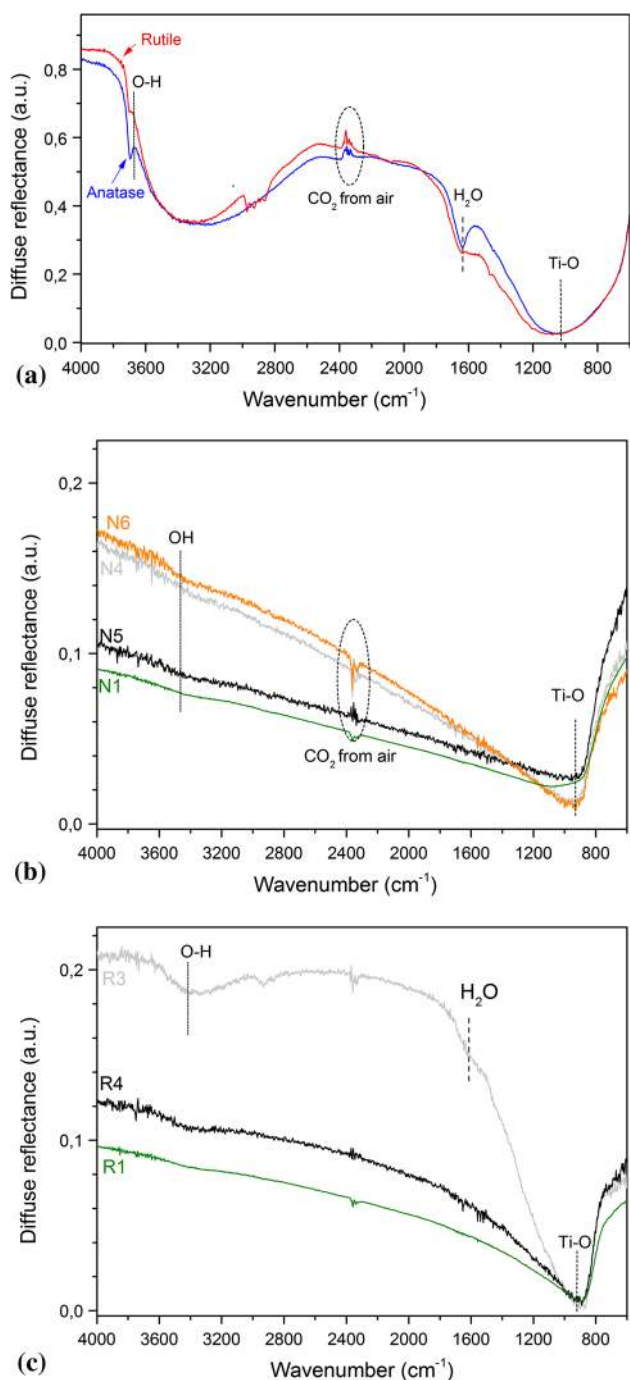
Fig. 10 Photocatalytic degradation of the RB solution under UV irradiation in the presence of (a) anatase coatings; (b) rutile coatings (degradation of RB solution without any TiO_2 coating (blank test) is also shown; "C_0" is the RB initial concentration after dark test (μmol/L) and "C" is the RB concentration (μmol/L) at irradiation time t (h))

Moreover, the band between 2900 and 2800 cm^{-1}, which was already observed in the rutile powder and corresponded to the powder impurities, was found only in the R3 coating and not in the other coatings that were sprayed with more energetic spray parameters.

3.6 Photocatalytic Performance of the Coatings

3.6.1 Photocatalytic Degradation of the Aqueous RB Solution. The degradation of the aqueous RB solution under UV irradiation in the presence of the suspension-sprayed coatings is shown in Fig. 10. During the dark test, the amount of adsorbed RB on the each coating surface was relatively low, less than 2.5% of the RB concentration being adsorbed. As can be seen in Fig. 10(b), almost no dye degradation was recorded in the absence of the coatings during the blank test. In the presence of the coatings, the photocatalytic degradation (C/C_0) showed different rates as a function of the coating. With anatase coatings, the removal of RB solution varied in a wide

Fig. 9 DRIFT spectra of TiO_2 of (a) raw powders, (b) selected anatase coatings, and (c) selected rutile coatings

3600-3200 cm^{-1} and the peaks between 1660 and 1630 cm^{-1} that could be attributed to OH modes and water molecules, respectively, were less intense. A greater extent of hydroxylation was observed for the coatings produced at the highest λ of 1.3, i.e., for the N4, N6, and R3 coatings. In the IR spectra of the R3 rutile samples, the peak intensities of the hydroxyl groups and physisorbed water were obviously greater than for other coatings.
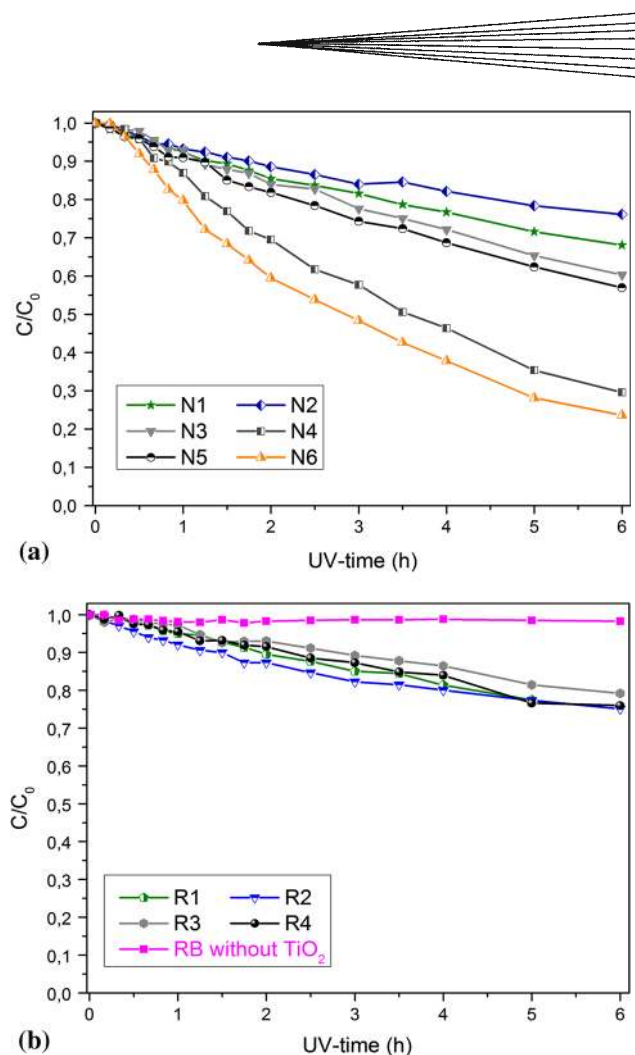
Table 3 Photocatalytic decomposition (discoloration) of RB in the presence of suspension-sprayed coatings using different tests (the decomposition (discoloration) of the RB due to the photolysis under UV irradiation is also given)

Coating/sample	Degradation of RB solution after 6 h UV			Discoloration of impregnated RB			
				Absolute color tonality (a^*) at			
	Removal, %	Rate constant, h^{-1}	Correlation coefficient (R^2)	$T_{UV} = 0$ min	$T_{UV} = 30$ min	Rate constant, min^{-1}	Correlation coefficient (R^2)
N1	31.9	0.0677	0.9957	…	…	…	…
N2	23.9	0.0551	0.9846	…	…	…	…
N3	39.7	0.0833	0.9980	14.58	2.06	0.0720	0.9952
N4	70.4	0.1960	0.9944	16.92	0.33	0.1331	0.9982
N5	43.7	0.0951	0.9985	12.21	2.11	0.0544	0.9973
N6	76.4	0.2453	0.9983	22.44	0.60	0.1379	0.9897
R1	22.5	0.0512	0.9977	…	…	…	…
R2	24.9	0.0562	0.9718	…	…	…	…
R3	20.8	0.0388	0.9933	17.81	0.81	0.1246	0.9796
R4	24.0	0.0475	0.9934	9.78	3.48	0.0251	0.9571
RB without TiO_2 (blank test) 1.7 (uncoated steel)	…	…	…	10.41 (uncoated ceramic)	10.64	$2.91 \cdot 10^{-4}$	…
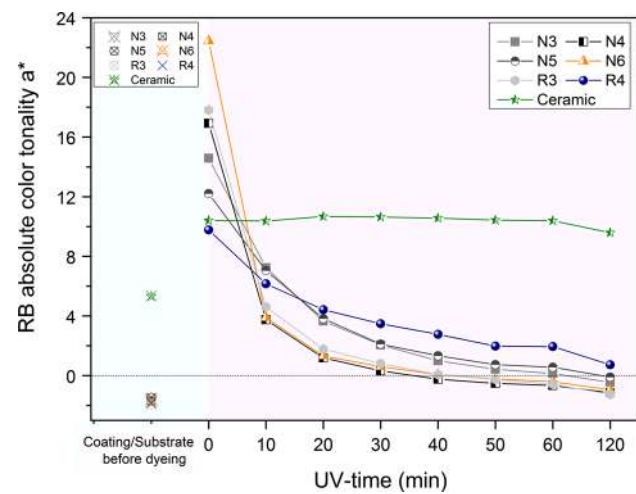
Fig. 11 Modification of the RB absolute color tonality (a^*) on the sprayed coatings and uncoated ceramic substrate during UV irradiation (color tonality of the sprayed coatings and substrate before dyeing is also shown)

range from about 24% up to 77%, whereas with rutile coatings, the degradation of the RB was 20-25% (Table 3).

The photocatalytic degradation of the RB follows the Langmuir-Hinshelwood first-order kinetics described by the equation:

$$-\frac{dC}{dt} = k'C \qquad \text{(Eq 5)}$$

The integration of Eq 5 gives

$$\ln \frac{C_0}{C} = k't, \qquad \text{(Eq 6)}$$

where C_0 is the initial concentration of RB after the dark test (μmol/L), C is the RB concentration (μmol/L) at irradiation time t (h), t is the irradiation time (h), and k' is the apparent rate constant of photocatalytic activity (h^{-1}).

From the slope of the plot of $\ln(C_0/C)$ versus time, the rate constants k' and their correlation coefficients (R^2) can be determined (Table 3). A higher value of the rate constant indicates faster photocatalytic degradation of the RB.

3.6.2 Discoloration of the Impregnated RB. The colorimetric measurements allowed the ability of the suspension-sprayed titania surfaces to degrade the impregnated RB under UV irradiation to be estimated. The UV light was maintained until full disappearance of the pink color occurred. The modification of the RB absolute color tonality (a^*) during the UV irradiation on the coating surfaces and uncoated ceramic substrate is shown in Fig. 11. The values of a^* of the coatings and uncoated ceramic substrate before dyeing are also represented. Before RB impregnation, the color tonalities of the coatings were measured to be in the same range, between −1.47 and −1.96, whereas the ceramic substrate showed an absolute a^* of about 5.33. After impregnation with the RB solution, the coloration of the coatings occurred and the values of a^* increased to different values as a function of the coating (in the CIE Lab System, positive values indicate tones of red color). A higher value of a^* indicates a higher retention of the RB on the surface of the coating (Table 3). It is important to note that the capability of the coatings to retain RB is strongly influenced by the chemical properties of the coating surface, by the presence of microstructural heterogeneities (presence of pores, cracks, and regions with nanoagglomerated particles), and by the coating thickness and is less affected by the phase composition. Thus, the values of a^* after RB impregnation for anatase coatings were measured to be between 12.21 (for the N5 coating) and 22.44 (for the N6 coating). The values of a^* of impregnated rutile coatings were 17.81 for R3 and 9.78 for R4. The value of a^* increased to 10.41 for the impregnated uncoated substrate. When UV irradiation was applied, a strong decrease in the color tonality on the coating surfaces (Fig. 11) was recorded after only 10 min of irradiation; then the discoloration became slower. Nonetheless, with only one exception (sample R4), less than

120 min of UV irradiation was needed for the values of $a*$ to become negative (in the CIE Lab System, negative values denote tones of green color). It is noteworthy that the TiO_2 coatings sprayed in this work showed superior discoloration performance to those presented in our previous study (Ref 19). In the case of the uncoated ceramic substrate, only a very low change in the color tonality was observed. In the absence of active TiO_2, the complete discoloration of the RB requires at least 4 days of UV irradiation.

Presuming that the color tonality $a*$ is proportional to the amount of impregnated RB on the surface of a sample, it can be proposed that the photocatalytic activity of a coating during the photocatalytic discoloration of the RB follows an equation similar to that described by Langmuir-Hinshelwood first-order kinetics. Equation 6 adapted to color tonality $a*$ can be described as

$$\ln \frac{a_0^*}{a^*} = k'_{a*}t, \qquad \text{(Eq 7)}$$

where a_0^* is the initial color tonality at $t = 0$ min of UV irradiation, $a*$ is the color tonality at irradiation time t (min), and k'_{a*} is the apparent rate constant of RB discoloration (min^{-1}). From the slope of the plot of $\ln(a_0^*/a^*)$ versus time, the rate constants k'_{a*} and their correlation coefficients (R^2) can be determined (Table 3). Higher values of the rate constants indicate faster discoloration of the impregnated RB on the surface of a photocatalytically active sample.

4. Discussion of the Influence of Coating Properties on Photocatalytic Performance

4.1 Coating Microstructures

As shown in the cross-sectional micrographs in Fig. 3 and 4, the microstructure of the suspension-sprayed coatings could be tailored by an appropriate choice of the spray parameters. The substrate type (stainless steel or ceramic) was found to have no notable influence on the coating microstructure. Spraying at higher gas flow rates and smaller spray distances mainly resulted in coatings with dense, homogeneous microstructures consisting of well-melted particles. Nonetheless, because of high thermal and relaxation stresses, the formation of cracks in thick coatings was evident. Improvement of the cooling modes or spraying of coatings of lower thickness (~50 μm) should result in the formation of crack-free coatings. For the photocatalytic applications, spraying of thin coatings can be very advantageous because the photocatalytic phenomenon mostly occurs on the surface or near-subsurface region of the coatings.

The bimodal microstructure with well-melted zones and regions of nano-sized agglomerated particles was produced using lower gas flow rates or larger spray distances. The nano-sized particles resulted from the partially melted or untreated particles. The presence of nanostructured zones significantly improved the photocatalytic

performance of the coatings. Microstructural defects, i.e., cracks and pores, observed in the microstructure of suspension-sprayed HVOF coatings mainly appeared at small spray distances. The presence of the porosity is considered to be helpful in increasing the photocatalytic activity of thermally sprayed coatings (Ref 21, 28). The presence of the cracks can allow better penetration of the pollutant solution into the bulk of the coating, but it can be detrimental because the light absorption can be significantly reduced in the cracks and the pollutant can penetrate deep into the coating microstructure; consequently, not all the pollutant can be photocatalytically degraded.

On the top surface (Fig. 5 and 6), different particles showing different thermal histories during spraying were observed in the SEM micrographs: fine micron-sized splats coming from the well-melted particles, agglomerated submicron particles resulting from partially melted particles, spherical particles with diameters ranging from several hundreds of nanometer up to a few micron (these particles melted and cooled down before reaching the substrate or the already-deposited particles), nano-sized agglomerated particles that only traversed the cool regions of the supersonic flame and arrived on the substrate in a
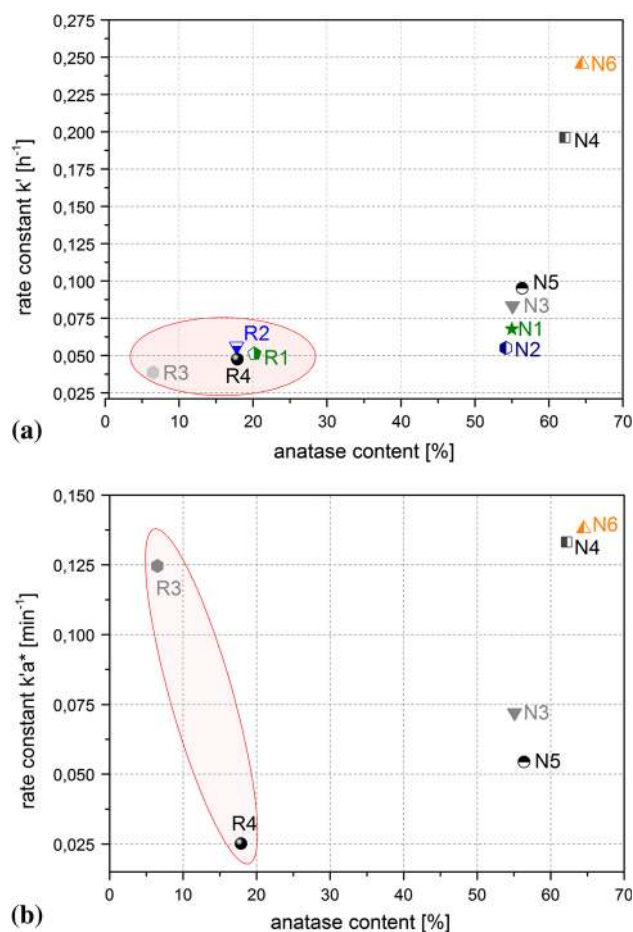

Fig. 12 Variation of rate constant k' (a) and rate constant k'_{a*} (b) as a function of anatase content

partially melted state, and recrystallized nanograins. In the case of spraying with high gas flow rates and small spray distances (N1 and R1 samples), splats were predominantly observed. With lower flow rates and larger spray distances, submicron- and nano-sized particles were mostly found. The presence of these particles will increase the specific surface area of the coating, allowing for improved light absorption, photoexcitation, generation of electron-hole pairs, and formation of photoactive radicals (ions) for initiation of the photocatalytic reactions. They also lead to better interaction between the coating and different ad-sorbed pollutant molecules. Thus, the specific top surface morphologies of the sprayed coatings that cannot be obtained by other deposition techniques are of great interest for photocatalytic applications.

4.2 Crystalline Phases

It is generally affirmed that anatase is the most desired phase for photocatalytic applications. Accordingly, the anatase-based materials were mainly used to produce photocatalytically active titania coatings and spraying of rutile suspensions has, with some exceptions (Ref 34, 35), been largely ignored. Besides the microstructure, the phase composition of the coating is also influenced by the spray parameters and to a lesser extent by the nature of the substrate. In addition to the flow rates and the spray distance, the role of the cooling rate and the substrate temperature in the retention of the anatase in the suspension-sprayed titania coatings has been confirmed by several authors (Ref 35, 47).

In the current work, a high content of anatase, from 55 to 65%, was retained in the coatings (Table 1), the highest value corresponding to the coating sprayed at low gas flow rates and a large spray distance (N6 and N4 anatase samples). If the coatings were of sufficient mechanical stability and suffered no degradation/disintegration during photocatalytic testing, then from an economical point of view the less energetic spray parameters (i.e., low gas flow rates) would be preferred for the production of photocatalytically active titania coatings.

In the case of the coatings prepared from the rutile suspension, the amount of anatase varied from about 7 to 20%, which was higher than the value published in the authors' previous study (Ref 34). Unlike in the case of the coatings produced from the anatase suspension, spraying at low gas flow rates (R3 rutile sample) resulted in the formation of a low amount of anatase phase, whereas spraying at higher gas flow rates and a smaller spray distance yielded coatings with high anatase contents (R1 rutile sample).

It is generally assumed that the anatase phase is present in the unmelted particles or results from nucleation from melted particles and very fast cooling because of its lower Gibbs free energy. The mechanism of anatase/rutile formation depends on the particle size and undercooling solidification, as described elsewhere (Ref 43, 47). Other authors (Ref 27) proposed that at higher impact velocity, a higher anatase content can be retained due to an enhancement in splat flattening and consequently to a higher splat solidification rate. Yang et al. (Ref 48)

showed that post-treatment of the anatase coatings at temperatures higher than 600 °C involved a significant phase transformation from anatase to rutile as well as an increase in the grain sizes.

Because the anatase/rutile transformation in the coating sprayed from an anatase suspension has been discussed extensively in the literature, only the anatase formation and anatase/rutile transformation occurring during spraying of a rutile suspension are presented here. When a rutile suspension is sprayed, small agglomerates of particles are formed after injection into the HVOF flame and vaporization of the water carrier fluid. The particles entering the hot zones of the flame agglomerate, melt, or even vaporize. The melted particles reach the substrate in the liquid state, forming micron-sized splats on impingement. The vaporized particles start to condense, and grain nuclei can be formed. When the substrate is positioned at a very short distance away, due to the high impact velocity, some of the nuclei crystallize as anatase grains. As the spray distance is increased, the anatase grains transform into rutile before reaching the substrate. The particles entering the colder zones of the HVOF flame can be partially melted; as the spraying distance increases, they start to resolidify before impacting the substrate. On the other hand, because of the thermophoresis phenomenon (Ref 42), the very small particles are pushed to the external zones of the flame and reach the substrate mostly in an unmelted state ("overspray" particles).

4.3 Influence of the Anatase Content on the Photocatalytic Activity

In the majority of the studies published, the photocatalytic performance of titania is correlated with the anatase content. In the present study, when the photocatalytic activity was estimated by the degradation of the RB solution, after 6 h of UV irradiation, the amount of RB removed was in the range 24-77% in the presence of the anatase coatings and 21-25% in the presence of the rutile coatings. The variation in the rate constant k' versus the anatase content (determined by XRD diffraction) is plotted in Fig. 12(a). At first sight, it can be clearly seen that the coatings produced from an anatase suspension were better photocatalysts than those obtained from a rutile suspension were. The values of k' versus anatase content for the rutile coatings were quite similar, whereas the k' values for the anatase coatings were much more dispersed, although the anatase content varied over a relatively narrow range. Moreover, the k' values of the N1 and N2 anatase coatings were almost the same as those of the R1 and R2 rutile coatings. Consequently, no direct correlation between the k' and the anatase content estimated by XRD diffraction could be established.

When the photocatalytic activity of the coatings was tested by discoloration of the impregnated RB on the coating surface, it was observed that the coatings were very active with rate constants k'_{a*} significantly higher than the rate constants k'. In contrast to the previous photocatalytic test results, the R3 rutile coating, which showed the lowest activity during degradation of RB solution,
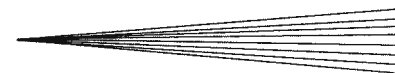
exhibited the highest activity for the degradation of impregnated RB. N3 and N5 anatase coatings changed their positions on the activity scale; only the N6 and N4 anatase coatings showed the best activities in both photocatalytic tests.

The dependency of the k'_{a*} rate versus anatase content (estimated by XRD diffraction) is shown in Fig. 12(b). It is noteworthy that the R3 rutile coating (containing only ~7% anatase) allowed for a faster discoloration of the RB than either the R4 rutile coating (with ~18% anatase) or the N3 and N5 anatase coatings (~55-56% anatase) did. The discrepancy between the photocatalytic performance of the coatings and the anatase content (as determined by XRD diffraction) was considerable for this photocatalytic test. Yang et al. (Ref 48) confirmed that the titania coatings can present a low photocatalytic activity even though they mainly consist of the anatase phase. They proposed that during transformation of anatase to rutile, the rutile grains first nucleate on the surfaces of the anatase nanoparticles and then growth of rutile and formation of a shell of rutile phase covering the anatase core occur.

A better correlation between the photocatalytic performance and the anatase content can be established when the phase compositions of the coatings are evaluated by Raman spectroscopy (Fig. 6). The more anatase on the surface, the better the photocatalytic activity is. Similar results were obtained by Burlacov et al. (Ref 32). This correlates well for the coatings produced from the anatase suspension, whereas it could not be verified by the discoloration of the impregnated RB on the rutile samples for the coatings obtained from the rutile suspension.

4.4 Influence of Other Coating Characteristics on the Photocatalytic Activity

Much research has been devoted to the preparation of thermally sprayed titania coatings with high anatase contents. Finely dispersed particles in a suspension allowed preparation of coatings with high anatase contents. Nonetheless, as shown in the present work and confirmed by other authors (see, e.g., Ref 20, 28, 34, 35, 48), other parameters must be considered for the clarification of the photocatalytic activity of sprayed coatings:

– Parameters related to the photonic processes: UV light absorption, photogeneration of electron pairs, and photoreactions with production of active radicals; and

– Parameters related to the physicochemical processes: presence of hydroxyl groups on the coating surface and interaction of the pollutant with the coating.

From the UV-Vis spectroscopy measurements (Fig. 7), it could be concluded that light absorption of the most active anatase samples (N6 and N4) and the rutile sample R3 would correspond better to the UV light conditions used for the photocatalytic tests. The beneficial role played by the presence of hydroxyl groups on the photocatalytic performance of the coatings has already been mentioned in several works (Ref 31, 48). As shown in the IR spectra (Fig. 9), a greater extent of hydroxylation was observed on the surfaces of N6, N4, and R3 samples. The greater extent of hydroxylation on the surface can explain the better performance of the R3 sample compared with other rutile or some anatase coatings after impregnation with the dye. Nonetheless, the presence of a higher content of weakly bonded water could negatively influence the efficiency of the R3 coating during degradation of the RB solution (Ref 31). The presence of surface contaminants, as observed in the IR spectra of the R3 sample, could also contribute to a decrease in the photocatalytic performance of this coating. The coating thickness could also contribute to the photocatalytic response (with a thinner coating expected to be more advantageous). This effect will be studied more closely in future research projects.

5. Conclusions

Thermal spraying with suspensions was applied to produce photocatalytically active titania coatings starting from two commercially available anatase and rutile submicron powders. All the coatings showed photocatalytical activity, but the performance differed significantly and depended on the phase composition as well as other factors. The presence of anatase in the coating was found to be necessary, but no direct correlation between the degradation rate and the phase composition could be ascertained. Coatings sprayed from an appropriate rutile suspension were found to present a photocatalytic activity comparable with that of coatings sprayed from the anatase suspension. Additional parameters related to the structural characteristics of the coatings and to the photocatalytic test should be considered. When the photocatalytic activity of a coating is evaluated, attention also has to be paid to other parameters related to the coating microstructure, surface morphology, thickness, and surface hydroxylation as well as to the capability of the coating to absorb the light, the ability of the coating to interact with the pollutant, and the method used for degradation of the pollutant. Coatings with greater extents of hydroxylation and lower physisorbed water contents on their surfaces showed better photocatalytic performance.

References

1. A. Fujishima and K. Honda, Electrochemical Photolysis of Water at a Semiconductor Electrode, *Nature*, 1972, **238**, p 37-38

2. J.-M. Herrmann, Heterogeneous Photocatalysis: Fundamentals and Applications to the Removal of Various Types of Aqueous Pollutants, *Catal. Today*, 1999, **53**, p 115-129

3. A. Mills and S. Le Hunte, An Overview of Semiconductor Photocatalysis, *J. Photochem. Photobiol. A*, 1997, **108**, p 1-35

4. A. Fujishima, T.N. Rao, and D.A. Tryk, Titanium Dioxide Photocatalysis, *J. Photochem. Photobiol. C*, 2000, **1**, p 1-21

5. K. Hashimoto, H. Irie, and A. Fujishima, TiO₂ Photocatalysis: A Historical Overview and Future Prospects, *Jpn. J. Appl. Phys.*, 2005, **44**, p 8269-8285

6. K. Nakata and A. Fujishima, TiO₂ Photocatalysis: Design and Applications, *J. Photochem. Photobiol. C*, 2012, **13**, p 169-189

7. U. Diebold, The Surface Science of Titanium Dioxide, *Surf. Sci. Rep.*, 2003, **48**, p 53-229

8. D.O. Scanlon, C.W. Dunnill, J. Buckeridge, S.A. Shevlin, A.J. Logsdail, S.M. Woodley, C. Richard, A. Catlow, M.J. Powell, R.G. Palgrave, I.P. Parkin, G.W. Watson, T.W. Keal, P. Sherwood, A. Walsh, and A.A. Sokol, Band Alignment of Rutile and Anatase TiO₂, *Nat. Mater.*, 2013, **12**, p 798-801

9. D. Reyes-Coronado, G. Rodríguez-Gattorno, M.E. Espinosa-Pesqueira, C. Cab, R. de Coss, and G. Oskam, Phase-Pure TiO₂ Nanoparticles: Anatase, Brookite and Rutile, *Nanotechnology*, 2008, **19**, p 145605

10. Y.R. Park and K.J. Kim, Structural and Optical Properties of Rutile and Anatase TiO₂ Thin Films: Effects of Co Doping, *Thin Solid Films*, 2005, **484**(1-2), p 34-38

11. X.-M. Song, J.-M. Wu, and M. Yan, Photocatalytic Degradation of Selected Dyes by Titania Thin Films with Various Nanostructures, *Thin Solid Films*, 2009, **517**, p 4341-4347

12. S. Tanemura, L. Miao, P. Jin, K. Kaneko, A. Terai, and N. Nabatova-Gabain, Optical Properties of Polycrystalline and Epitaxial Anatase and Rutile TiO₂ Thin Films by RF Magnetron Sputtering, *Appl. Surf. Sci.*, 2003, **212-213**, p 654-660

13. D.C. Hurum, A.G. Agrios, and K.A. Gray, Explaining the Enhanced Photocatalytic Activity of Degussa P25 Mixed Phase TiO₂ Using EPR, *J. Phys. Chem. B*, 2003, **107**(19), p 4545-4549

14. D.C. Hurum, K.A. Gray, T. Rajh, and M.C. Thurnauer, Recombination Pathways in the Degussa P25 formulation of TiO₂: Surface Versus Lattice Mechanisms, *J. Phys. Chem. B*, 2005, **109**, p 977-980

15. G. Li and K.A. Gray, The Solid-Solid Interface: Explaining the High and Unique Photocatalytic Reactivity of TiO₂-Based Nanocomposite Materials, *Chem. Phys.*, 2007, **339**, p 173-187

16. L.-M. Berger, *Titanium Oxide—New Opportunities for an Established Coating Material, Thermal Spray Solutions: Advances in Technology and Applications*, May 10-12, 2004, Osaka, Japan, DVS-Verlag GmbH, Düsseldorf, 2004, on CD-ROM

17. G.-J. Yang, C.-J. Li, Y.-Y. Wang, and C.-X. Li, Dominant Microstructural Feature over Photocatalytic Activity of High Velocity Oxy-Fuel Sprayed TiO₂ Coating, *Surf. Coat. Technol.*, 2007, **202**(1), p 63-68

18. T. Kanazawa and A. Ohmori, Behavior of TiO₂ Coating Formation on PET Plate by Plasma Spraying and Evaluation of Coating's Photocatalytic Activity, *Surf. Coat. Technol.*, 2005, **197**, p 45-50

19. F.-L. Toma, L.-M. Berger, D. Jacquet, D. Wicky, I. Villaluenga, Y.R. de Miguel, and J.S. Lindeløv, Comparative Study on the Photocatalytic Behaviour of Titanium Oxide Thermal Sprayed Coatings from Powders and Suspensions, *Surf. Coat. Technol.*, 2009, **203**, p 2150-2156

20. P. Ctibor, V. Stengl, I. Pís, T. Zahoranová, and V. Nehasil, Plasma Sprayed TiO₂: The Influence of Power of an Electric Supply on Relations among Stoichiometry, Surface State and Photocatalytic Decomposition of Acetone, *Ceram. Int.*, 2012, **38**, p 3453-3458

21. P. Ctibor, Z. Pala, J. Sedlacek, V. Stengl, T. Zahoranova, and V. Nehasil, Titanium Dioxide Coatings Sprayed by a Water-Stabilized Plasma Gun (WSP) with Argon and Nitrogen as the Powder Feeding Gas: Differences in Structural, Mechanical and Photocatalytic Behavior, *J. Therm. Spray Technol.*, 2012, **21**(3-4), p 425-434

22. A. Ohmori, K. Nakade, and Y. Yamamoto, Photocatalytic Decomposition of Ammonia by Thermal Sprayed TiO₂ Coatings, Thermal Spray 2003: Advancing the Science & Applying the Technology, *Proceedings of the International Thermal Spray Conference & Exhibition ITSC 2003*, C. Moreau and B. Marple, Eds., ASM International, Materials Park, Ohio, 2003, p 189-193

23. F.L. Toma, G. Bertrand, S. OkChwa, D. Klein, H. Liao, C. Meunier, and C. Coddet, Microstructure and Photocatalytic Properties of Nanostructured TiO₂ and TiO₂-Al Coatings Elaborated by HVOF Spraying for the NOₓ Removal, *Mater. Sci. Eng. A*, 2006, **417**, p 56-62

24. F.-L. Toma, G. Bertrand, S.O. Chwa, C. Meunier, D. Klein, and C. Coddet, Comparative Study on the Photocatalytic Decomposition of Nitrogen Oxides using TiO₂ Coatings Prepared by Conventional Plasma Spraying and Suspension Plasma Spraying, *Surf. Coat. Technol.*, 2006, **200**, p 5855-5862

25. F.L. Toma, D. Sokolov, G. Bertrand, D. Klein, C. Coddet, and C. Meunier, Comparison of the Photocatalytic Behavior of TiO₂ Coatings Elaborated by Different Thermal Spraying Processes, *J. Therm. Spray Technol.*, 2006, **15**(4), p 576-581

26. H. Lee, Ch Choi, C. Lee, and H. Kim, Photocatalytic Properties of Nanostructured TiO₂ Plasma Sprayed Coating, *Surf. Coat. Technol.*, 2003, **173**, p 192-200

27. J. Colmenares-Angulo, S. Zhao, C. Young, and A. Orlov, The Effects of Thermal Spray Technique and Post-Deposition Treatment on the Photocatalytic Activity of TiO₂ Coatings, *Surf. Coat. Technol.*, 2009, **204**, p 423-427

28. C. Zhang, U. Chaudhary, S. Das, A. Godavarty, and A. Agarwal, Effect of Porosity on Photocatalytic Activity of Plasma-Sprayed TiO₂ Coating, *J. Therm. Spray Technol.*, 2013, **22**(7), p 1193-1200

29. G.-J. Yang, C.-J. Li, F. Han, and A. Ohmori, Microstructure and Photocatalytic Performance of High Velocity Oxy-Fuel Sprayed TiO₂ coatings, *Thin Solid Films*, 2004, **466**, p 81-85

30. F.-L. Toma, G. Bertrand, D. Klein, C. Coddet, and C. Meunier, Nanostructured Photocatalytic Titania Coatings Formed by Suspension Plasma Spraying, *J. Therm. Spray Technol.*, 2006, **15**(4), p 587-592

31. F.-L. Toma, G. Bertrand, S. Begin, C. Meunier, O. Barres, D. Klein, and C. Coddet, Microstructure and Environmental Functionalities of TiO₂-Supported Photocatalysts Obtained by Suspension Plasma Spraying, *Appl. Catal. B*, 2006, **68**, p 74-84

32. I. Burlacov, J. Jirkovský, M. Müller, and R.B. Heimann, Induction Plasma-Sprayed Photocatalytically Active Titania Coatings and their Characterisation by Micro-Raman Spectroscopy, *Surf. Coat. Technol.*, 2006, **201**, p 255-264

33. G. Bolelli, V. Cannillo, R. Gadow, A. Killinger, L. Lusvarghi, and J. Rauch, Properties of High Velocity Suspension Flame Sprayed (HVSFS) TiO₂ coatings, *Surf. Coat. Technol.*, 2009, **203**, p 1722-1732

34. S. Kozerski, F.-L. Toma, L. Pawlowski, B. Leupolt, L. Latka, and L.-M. Berger, Suspension Plasma Sprayed TiO₂ Coatings Using Different Injectors and Their Photocatalytic Properties, *Surf. Coat. Technol.*, 2010, **205**, p 980-986

35. E. Bannier, G. Darut, E. Sánchez, A. Denoirjean, M.C. Bordes, M.D. Salvador, E. Rayón, and H. Ageorges, Microstructure and Photocatalytic Activity of Suspension Plasma Sprayed TiO₂ Coatings on Steel and Glass Substrates, *Surf. Coat. Technol.*, 2011, **206**, p 38-386

36. C.-J Li, G.-J. Yang, X.-C. Huang, W. Li, and A. Ohmori, Formation of TiO₂ Photocatalyst Through Cold Spraying, Thermal Spray 2004: Advances in Technology and Application, *Proceedings of the International Thermal Spray Conference & Exhibition ITSC 2004*, May 10-12, Osaka, Japan, DVS-Verlag GmbH, Düsseldorf, 2004, on CD-ROM Version

37. M. Yamada, H. Isago, N. Nakano, and M. Fukumoto, Cold Spraying of TiO₂ Photocatalyst with Nitrogen Process Gas, *J. Therm. Spray Technol.*, 2010, **19**(6), p 1218-1223

38. I. Ivanova, J. Schneider, H. Gutzmann, J.-O. Kliemann, F. Gärtner, T. Klassen, D. Bahnemann, and C.B. Mendive, Photocatalytic Degradation of Oxalic and Dichloroacetic Acid on TiO₂ Coated Metal Substrates, *Cat. Today*, 2013, **209**, p 84-90
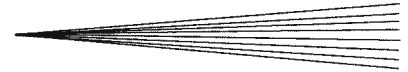
39. H. Gutzmann, J.-O. Kliemann, R. Albrecht, F. Gärtner, T. Klassen, F.-L. Toma, L.-M. Berger, and B. Leupolt, Evaluation of the Photocatalytic Activity of TiO$_2$-Coatings Prepared by Different Thermal Spray Techniques, Thermal Spray: Global Solutions for Future Applications, *Proceedings of the 2010 International Thermal Spray Conference, Singapore*, May 3-5, 2010, DVS 264, 2010, CD-ROM Version

40. F.-L. Toma, L.-M. Berger, S. Langner, and T. Naumann, Suspension Spraying—The Potential of a New Spray Technology, *Therm. Spray Bull.*, 2010, **3**(1), p 24-29

41. L.-M. Berger, F.-L. Toma, and A. Potthoff, Thermal Spraying with Suspensions—An Economical Spray Process, *Therm. Spray Bull.*, 2013, **6**(2), p 98-101

42. P. Fauchais, V. Rat, J.-F. Coudert, R. Etchart-Salas, and G. Montavon, Operating Parameters for Suspension and Solution Plasma-Spray Coatings, *Surf. Coat. Technol.*, 2008, **202**(18), p 4309-4317

43. L. Pawlowski, Suspension and Solution Thermal Spray Coatings, *Surf. Coat. Technol.*, 2009, **203**, p 2807-2829

44. W.F. Zhang, Y.L. He, M.S. Zhang, Z. Yin, and Q. Chen, Raman Scattering Study on Anatase TiO$_2$ Nanocrystals, *J. Phys. D*, 2000, **33**, p 912-916

45. K.M. Reddy, S.V. Manorama, and A.R. Reddy, Bandgap Studies on Anatase Titanium Dioxide Nanoparticles, *Mater. Chem. Phys.*, 2002, **78**, p 239-245

46. H. Nakajima, T. Mori, Q. Shen, and T. Toyoda, Photoluminescence Study of Mixtures of Anatase and Rutile TiO$_2$ Nanoparticles: Influence of Charge Transfer between the Nanoparticles on Their Photoluminescence Excitation Bands, *Chem. Phys. Lett.*, 2005, **409**(1-3), p 81-84

47. G. Mauer, A. Guignard, and R. Vaßen, Plasma Spraying of Efficient Photoactive TiO$_2$ Coatings, *Surf. Coat. Technol.*, 2013, **220**, p 40-43

48. G.-J. Yang, C.-J. Li, and Y.-Y. Wang, Phase Formation of Nano-TiO$_2$ Particles During Flame Spraying with Liquid Feedstock, *J Therm. Spray Technol.*, 2005, **14**(4), p 480-486

Peer Reviewed